nature communications

Article

https://doi.org/10.1038/s41467-025-59124-3

Potassium-stabilized metastable carbides and chalcogenides via surface chemical potential modulation

Received: 1 September 2024

Accepted: 9 April 2025

Published online: 24 April 2025

Check for updates

Fanpeng Chen[1,2], Chuanqi Cheng[1,2], Jiajun Wang[1], Yanran Han[1], Bo-Hang Zhao[1] ✉ & Bin Zhang[1] ✉

Metastable carbides and chalcogenides are attractive candidates for wide and promising applications. However, their inherent instability leads to synthetic difficulty and poor durability. Thus, the development of facile strategies for the controllable synthesis and stabilization of metastable carbides is still a great challenge. Here, taking metastable ε-Fe_2C as a case study, potassium ions (K^+) are theoretically predicted and experimentally reported to control the synthesis of metastable ε-Fe_2C from an Fe_2N precursor by increasing the surface carbon chemical potential (μ_C). The controllable synthesis and improved stability are attributed to the better-matched denitriding and carburizing rates and the impeded spillover of carbon atoms in metastable ε-Fe_2C with high carbon contents due to the enhanced surface μ_C. In addition, this strategy is suitable for synthesizing metastable γ′-MoC, MoN, 1*T*-MoS_2, 1*T*-$MoSe_2$, 1*T*-$MoSe_{2x}Te_{2(1-x)}$, and 1*T*-$Mo_{1-x}W_xSe_2$, highlighting the universality of the methodology. Impressively, gram-level scalable metastable ε-Fe_2C remains stable for more than 398 days in air. Furthermore, ε-Fe_2C exhibits remarkable olefin selectivity and durability for more than 36 h of continuous testing. This work not only demonstrates a facile, easily scalable, and general strategy for accessing various metastable carbides and chalcogenides but also addresses the synthetic difficulty and poor durability challenge of metastable materials.

Metastable carbides and chalcogenides are widely demanded in various fields[1–6]. For example, transition metal carbides (TMCs) with high carbon contents (e.g., ε-Fe_2C and γ′-MoC) are metastable carbide species that are promising candidates for CO_x hydrogenation, methanol reforming, and water–gas shift reactions[7–9]. However, the controllable synthesis of these metastable carbide species is still a great challenge[10,11]. In addition, the inevitable restructuring that always occurs during the catalytic process also leads to undesirable on-stream stability[12], creating additional obstacles for the practical application of metastable carbide species.

Generally, synthetic difficulty and poor operating stability are associated with chemical equilibrium[13,14], which is influenced by the Gibbs free energy change (ΔG) from a metastable state to a stable state. Under a specific system with the same temperature (T) and pressure, ΔG is related only to the chemical potentials (μ) of all the substances in the system, which are closely associated with the surface adsorbed species[15,16] (Fig. 1a). In terms of the reported strategies for constructing specific metastable carbides, μ is temporarily changed because of the extreme applied conditions (e.g., high pressure, rapid quenching, and narrow temperature range)[17,18]. However, the chemical potential difference ($\Delta\mu$) between the metastable and stable phases still drives structural evolution during catalytic operation. Specifically, for interstitial-type TMCs, the diffusion of carbon in the structure plays an important role in carbide phase conversion. For metastable carbides

[1]Department of Chemistry, Institute of Molecular Plus, School of Science, Tianjin University, Tianjin, China. [2]These authors contributed equally: Fanpeng Chen, Chuanqi Cheng. ✉e-mail: bhzhao@tju.edu.cn; bzhang@tju.edu.cn

https://doi.org/10.1038/s41467-025-59124-3

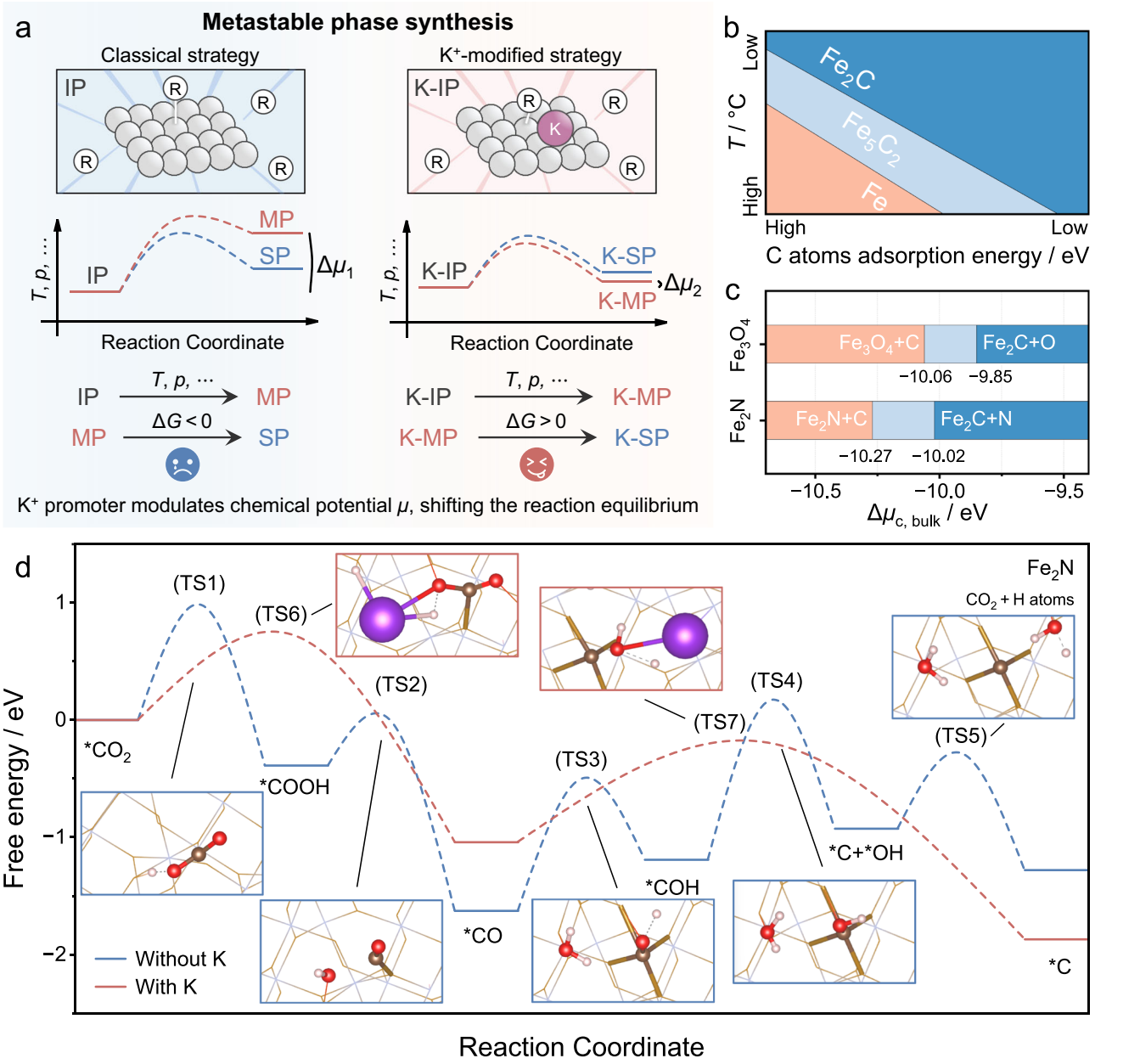

Fig. 1 | Calculation-guided design of metastable ε-Fe_2C. a Schematic of the classical strategy for synthesizing metastable species and our proposed K^+-modified strategy by modulating the chemical potential μ and reaction equilibrium. IP initial phase, R reactants, MP metastable phase, SP stable phase. **b** Schematic of the phase diagram of the Fe–C system. **c** DFT calculation of the bulk phase evolution ($\Delta\mu_C$), bulk over the Fe_3O_4 and Fe_2N precursors. **d** Free-energy diagram of the construction process over Fe_2N and K-Fe_2N under CO_2 and H_2 atmospheres. Purple: K, red: O, blue: N, pink: H, light brown: C, and brown: Fe. Visuals were produced with VESTA[50].

with high carbon concentrations, the lower surface carbon chemical potential (μ_C) under high-temperature catalytic conditions favors the diffusion of bulk carbon to form a relatively stable phase both thermodynamically and kinetically (e.g., ε-Fe_2C to χ-Fe_5C_2 or θ-Fe_3C, γ′-MoC to β-Mo_2C)[16,19,20]. Therefore, exploring a strategy to modulate the surface μ_C during both carbide synthesis and operation to prevent carbon loss is pivotal for the controllable synthesis and stabilization of metastable TMCs.

In this article, the synthesis of metastable ε-Fe_2C is chosen as a case study because of its predicted high activity but weak stability towards selective CO_2 hydrogenation to light olefins. Iron nitride (Fe_2N) was first selected as the precursor for subsequent carbonization through density functional theory (DFT) calculations because of its lowered carburizing barrier and similar crystal structure to that of the target ε-Fe_2C. DFT calculations were also employed to verify the feasibility of potassium ion (K^+) modulation of the surface-adsorbed carbon-containing species for enhancing the surface μ_C (Fig. 1a), which is beneficial for the controllable reconstruction of Fe_2N to ε-Fe_2C. Then, ε-Fe_2C was successfully obtained through in situ reconstruction of the designed K^+-modified Fe_2N loaded on carbon (K-Fe_2N@C). Moreover, the combined results of DFT calculations and operando characterizations demonstrate that the controllable construction of ε-Fe_2C is ascribed to the enhanced surface μ_C and the consequent better-matched denitriding and rates, which lowers the formation energy barrier of ε-Fe_2C and prevents carbon atom spillover. Furthermore, the K^+-promoted μ modulation strategy has been proven to be universal for the controllable synthesis of other metastable TMCs, nitrides, and chalcogenides (e.g., metastable γ′-MoC, MoN, 1T-MoS_2,

https://doi.org/10.1038/s41467-025-59124-3

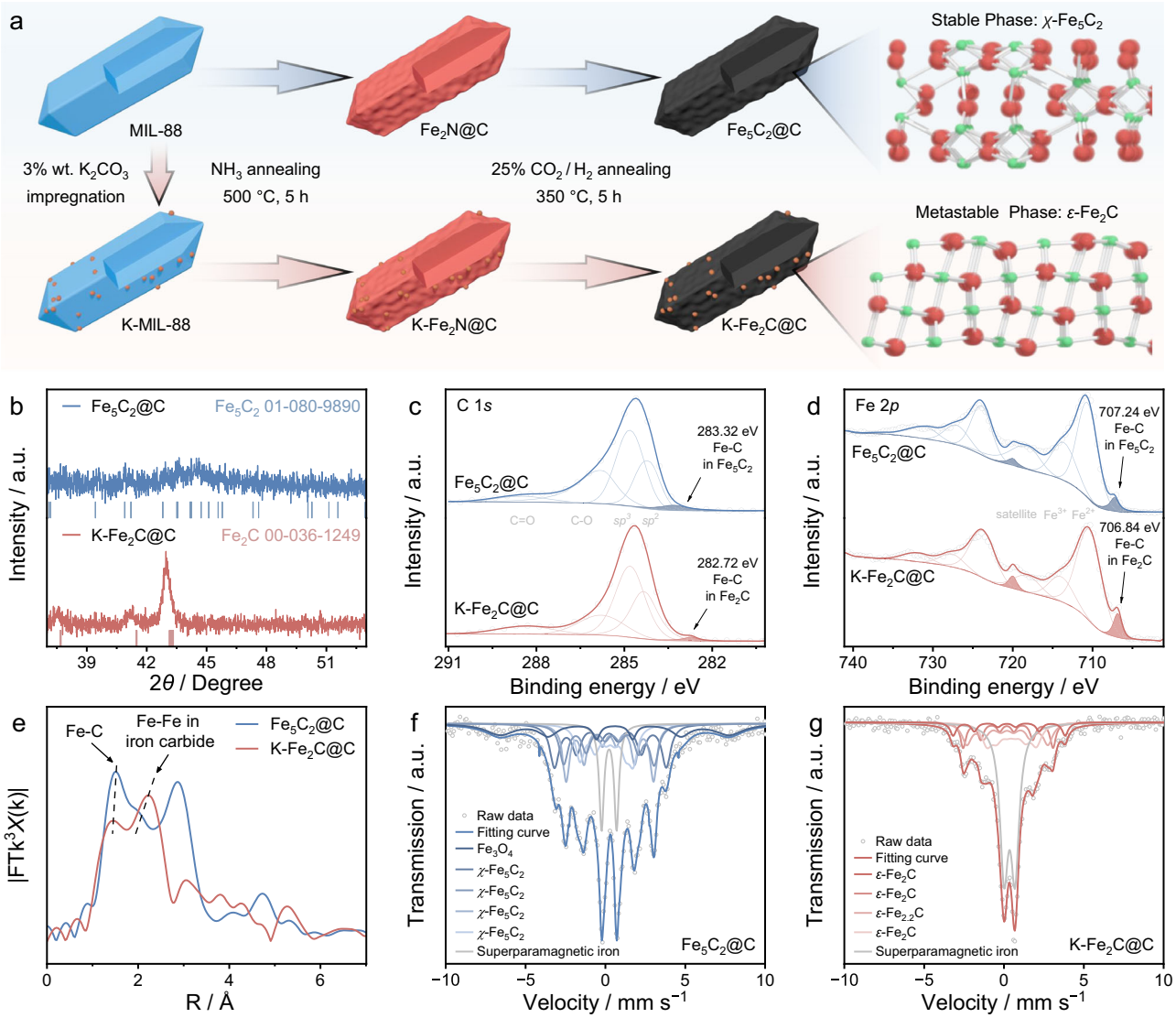

Fig. 2 | Synthesis and characterizations of metastable ε-Fe_2C. a Scheme for the synthesis of ε-Fe_2C from K-Fe_2N (red arrow: K^+-modified strategy). Red atoms: Fe, green atoms: C. Visuals of ε-Fe_2C and χ-Fe_5C_2 were produced with VESTA[50] and Blender. **b** XRD patterns of Fe_5C_2@C and K-Fe_2C@C. **c**, **d** XPS C1*s* spectra and Fe 2*p* spectra of Fe_5C_2@C and K-Fe_2C@C. **e** EXAFS spectra of Fe_5C_2@C and K-Fe_2C@C. **f**, **g** Mössbauer spectra of Fe_5C_2@C and K-Fe_2C@C. All "a.u." represents arbitrary units.

1*T*-$MoSe_2$, 1*T*-$MoSe_{2x}Te_{2(1-x)}$, and 1*T*-$Mo_{1-x}W_xSe_2$). Finally, as a proof-of-concept application, easily scalable ε-Fe_2C enables improved olefin selectivity (42.3%) and a prolonged lifetime of over 36 h.

Results

Design of K^+-modulated Fe_2N reconstruction for the synthesis of ε-Fe_2C

Metastable ε-Fe_2C is selected as the case study because it is theoretically predicted to be an appealing active species for CO_2 hydrogenation to light olefins, but still suffers from synthetic difficulty and instability concerns for most metastable materials. However, the instability of metastable materials makes their direct synthesis and stabilization highly challenging. Using the controllable synthesis of metastable ε-Fe_2C as a case study, carbonization kinetics are positively correlated with temperature (*T*), but the C atom adsorption energy of metastable ε-Fe_2C rapidly decreases with increasing *T* (Fig. 1b), resulting in difficulty in its synthesis and stabilization. Thus, two factors should be taken into consideration in the controllable synthesis and stabilization of ε-Fe_2C: (1) lowering the energy barrier of the carburization process to decrease *T* and (2) enhancing the surface μ_C (referred to as the negative shift in the μ_C value in this work) to increase carburization and prevent carbon loss from the bulk. Since we previously demonstrated that iron carbides can be a precursor, similar to Fe and/or Fe-based oxides, for the synthesis of iron carbides[7,21,22]. However, the specific principles for precursor selection and the mechanism of stabilized ε-Fe_2C synthesis remain unclear. Here, $\Delta\mu_{C,\,bulk}$ is defined as the energy barrier descriptor for the bulk carburization of different Fe-based precursors. The results of the DFT calculations indicated that the $\Delta\mu_C$ of the bulk of Fe_2N (−10.02 eV) is much lower than that of its Fe_3O_4 and Fe counterparts (−9.85, −9.03 eV) (Fig. 1c, Supplementary Figs. 1 and 2, and Supplementary Note 1), indicating that Fe_2N is a suitable precursor for constructing metastable ε-Fe_2C[20,23]. However, the formation trend of χ-Fe_5C_2 is still greater than that of the target ε-Fe_2C. Since the surface μ_C is highly related to the adsorbed carbon-containing intermediates, the K^+ promoter is adopted to further increase carbonization and improve durability by modifying the adsorbates and enhancing the surface μ_C during the reconstruction and operation process[24,25]. The feasibility of the K^+-modulation strategy was subsequently verified by the energy change profiles of the transition states (TSs) of the carbonization process (Fig. 1d and

https://doi.org/10.1038/s41467-025-59124-3

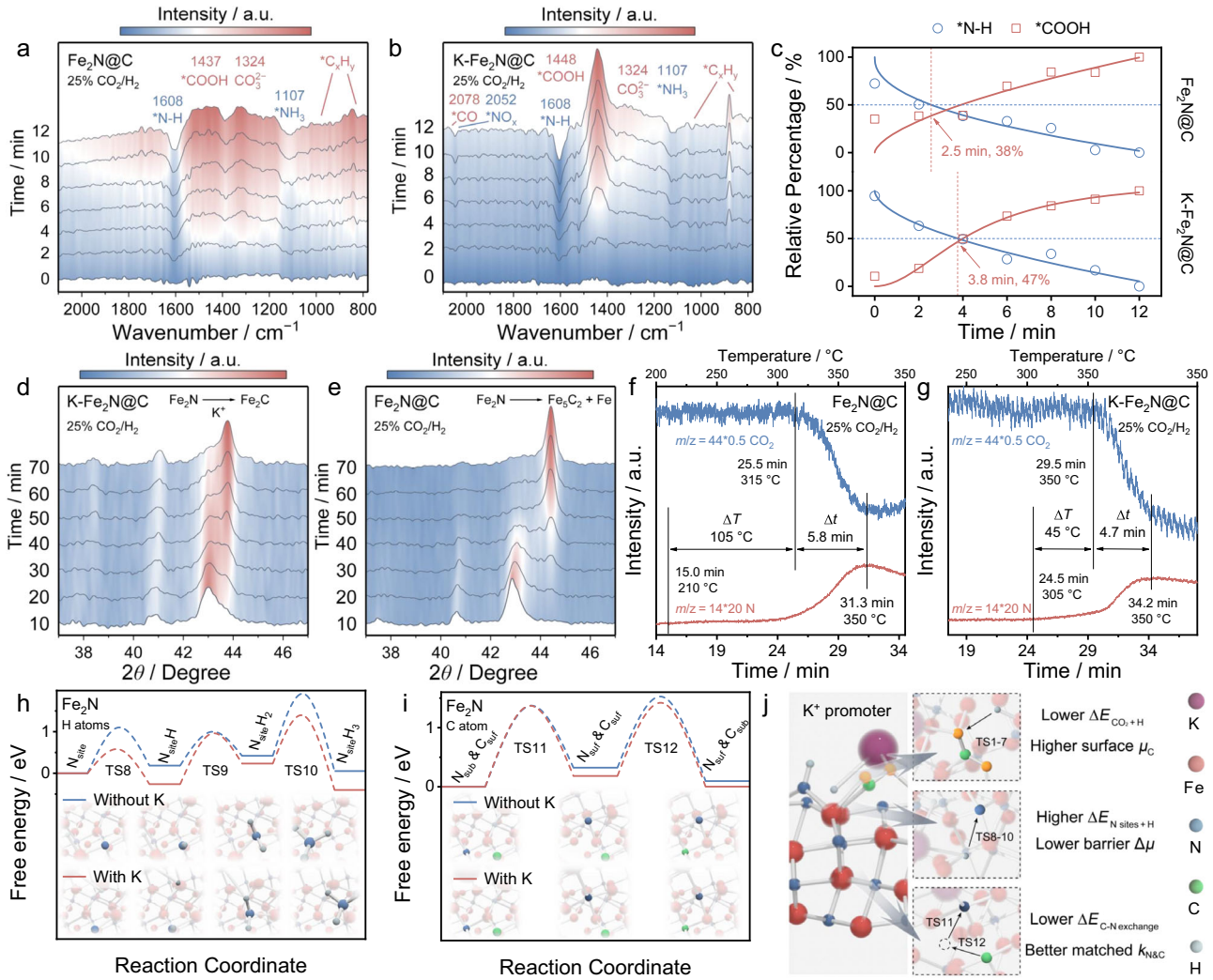

Fig. 3 | Mechanistic studies. a, **b** In situ DRIFTS spectra of Fe_2N@C (a) and K-Fe_2N@C (b) in a 25% CO_2/H_2 atmosphere at 0.1 MPa. **c** Time course of the relative percentage of the infrared bands of Fe_2N@C and K-Fe_2N@C. Solid lines were obtained by fitting signals according to the Hill equation[51,52]. **d**, **e** In situ XRD patterns of Fe_2N@C and K-Fe_2N@C recorded in 25% CO_2/H_2 at 350 °C and 0.1 MPa. **f** TPSR–MS profile of Fe_2N@C and **g** K-Fe_2N@C in a 25% CO_2/H_2 atmosphere at 0.1 MPa. "a.u." represents arbitrary units. **h**, **i** Free-energy diagram of the N site hydrogenation process and carbon–nitrogen atom exchange process over Fe_2N with or without K^+. **j** Scheme showing how the K^+ promoter affects the construction of the Fe_2C phase. Visuals were produced with VESTA[50] and Blender.

Supplementary Figs. 3–13). Owing to the oxygen affinity exhibited by K atoms (insets corresponding to TS6 and TS7 in Fig. 1d), the dehydration process generating *CO and *C is more favorable over Fe_2N with K^+ than that without K^+, demonstrating the easy formation of surface carbon species, thus leading to a lower carburizing T and higher surface μ_C (Supplementary Figs. 3 and 4 and Supplementary Note 3). These calculated results reveal that the K^+-modulated Fe_2N reconstruction strategy is promising for the controllable formation and subsequent stabilization of metastable ε-Fe_2C.

Synthesis and characterization of metastable ε-Fe_2C

To validate our calculation results, K-Fe_2N@C and its counterpart Fe_2N@C were synthesized via self-template impregnation-nitridation of the MIL-88 precursor with and without K_2CO_3 as the K^+ source, respectively (Fig. 2a). The peaks in the X-ray diffraction (XRD) patterns of the obtained materials matched well with those of Fe_2N (ICDD-PDF-4 no. 01-072-2126), demonstrating the successful preparation of the Fe_2N precursors (Supplementary Figs. 14–18, Supplementary Notes 4 and 5, and Supplementary Table 1). Next, these iron nitrides were carburized under a 25% CO_2/H_2 atmosphere at 350 °C for 5 h to form iron carbides. As illustrated in Fig. 2b, the diffraction peaks of the counterpart without K^+ are indexed to χ-Fe_5C_2 (ICDD-PDF-4 no. 01-080-9890) (denoted as Fe_5C_2@C), whereas those of ε-Fe_2C (ICDD-PDF-4 no. 00-036-1249), which features a similar crystal structure to that of the Fe_2N precursor, are obtained for the K^+-containing sample (denoted as K-Fe_2C@C). The above XRD results primarily prove the direct construction of metastable ε-Fe_2C species. X-ray photoelectron spectroscopy (XPS) was subsequently conducted to further identify the two obtained iron carbide species. The characteristic peaks with lower binding energies in the XPS C 1*s* spectra and Fe 2*p* spectra are typical signals of Fe–C bonds. The two groups of characteristic peaks over samples with and without the K^+ promoter are typically attributed to χ-Fe_5C_2 and ε-Fe_2C species, respectively (Fig. 2c, d, Supplementary Figs. 19 and 20, and Supplementary Note 6)[26–29]. Moreover, X-ray absorption spectroscopy (XAS) was employed to determine the local coordination environment of the as-prepared iron carbide samples. Fe K-edge XANES suggested that both samples exhibited similar oxidation states and had similar carbon atom neighbors with shorter Fe–C bonds around the central Fe atom (Supplementary Figs. 21 and 22). However, as evidenced by the extended X-ray absorption fine structure (EXAFS) spectra (Fig. 2e), the Fe–C coordination shells of K-Fe_2C@C (1.44 Å) are lower than those of Fe_5C_2@C (1.50 Å), whereas

the average first Fe−Fe shell bond length narrows from 2.08 Å over Fe_5C_2@C to 2.21 Å over K-Fe_2C@C[30,31]. These opposite trends confirm that a difference in the carbon content exists between these two carbide samples because the incorporation of more C atoms into the lattice shortens the Fe−C bonds and elongates the Fe−Fe bonds. Mössbauer spectroscopy, with high resolution for the chemical environment of the Fe atom, further proves the conversion from Fe_2N with K^+-modification to metastable ε-Fe_2C, whereas the main carbide phase of the K^+-free counterpart remains χ-Fe_5C_2 (Fig. 2f, g and Supplementary Table 2)[32]. These results together verify the successful construction of metastable ε-Fe_2C species and suggest that the reconstruction product of the Fe_2N precursor under a CO_2–H_2 atmosphere could be regulated from the stable χ-Fe_5C_2 phase to the metastable ε-Fe_2C phase via a simple K^+-modulation strategy.

Mechanistic studies on the K^+-mediated controllable synthesis of ε-Fe_2C

To gain insight into the mechanism of K^+-mediated Fe_2N selective reconstruction into metastable ε-Fe_2C, a series of in situ spectral techniques were used to monitor the evolution behaviors of Fe_2N@C and K-Fe_2N@C. For in situ diffuse reflectance infrared Fourier transform spectroscopy (DRIFTS), which detects changes in surface adsorbed species, the spectrum obtained when the temperature reached 350 °C under an Ar atmosphere was designated as the background, followed by time-dependent signal collection under a 25% CO_2/H_2 atmosphere (Fig. 3a–c). Although the intensities of the band at approximately 1448 cm^{-1} (*COOH), which is related to the surface μ_C, increase markedly over both samples, more significant *COOH bands compared with the signal of inert *CO_3^{2-} over K-Fe_2N@C than that over Fe_2N@C suggest that more carbon-containing species exist after K^+-modulation[33–36]. The higher surface carbon-species concentration over K-Fe_2N@C is also substantiated by the CO-temperature-programmed desorption (TPD) and in situ Raman spectra (Supplementary Figs. 23 and 24 and Supplementary Notes 7 and 8). These results primarily indicate that the K^+ promoter increases the surface μ_C and thermodynamically facilitates the synthesis of metastable ε-Fe_2C. In addition, the bands at 1608 cm^{-1} (*N–H) and 1107 cm^{-1} (*NH_3) were detected as inverted peaks during the acquisition time, indicating denitrification[37,38]. The 50% attenuation point of the *N–H species was subsequently used as a descriptor for denitrification kinetics[39]. As shown in Fig. 3c, it only takes 2.5 min for Fe_2N@C to reach the 50% attenuation point, whereas 3.8 min is needed for K-Fe_2N@C, at which the intensity percentages of *COOH, which is deemed the indicator of surface μ_C, are 38% and 47%, respectively. In other words, the K^+ promoter delays the denitrification process, making it match better with a high surface μ_C. The change in surface μ_N after K^+ modulation also supports this view (Supplementary Figs. 25 and 26 and Supplementary Note 9). In addition, the in situ XRD results provided further information on the crystal structure (Fig. 3d, e). For the K-Fe_2N@C precursor, the diffraction peaks of Fe_2N clearly shift to higher Bragg angles after 30 min at 350 °C because of the nitrogen spill, after which the predominant diffraction peak at 43.0° gradually vanishes as the profile shape of ε-Fe_2C becomes dominant. Conversely, the species construction over Fe_2N@C shifted to an earlier time and started after 17.2 min. The formation of χ-Fe_5C_2 species is accompanied by the typical diffraction of Fe (ICDD-PDF-4 no. 97-006-4795) at 44.5°, suggesting that the onset of denitrification is too premature to match carburization when K^+ is lacking. The in situ XRD results also indicate that there is a matching problem. Accordingly, a CO_2-H_2-temperature-programmed surface reaction with mass spectrometry (TPSR–MS) was conducted to further provide direct evidence of denitrification–carbonization kinetics (Fig. 3f, g, Supplementary Figs. 27 and 28, and Supplementary Note 10). The signal of N-related escaped species appears ca. 210 °C over Fe_2N@C, whereas CO_2 remains unactivated until 315 °C, reaching a temperature gap (ΔT) as wide as 105 °C (Fig. 3f), making the reconstruction of Fe_2N mismatched with the high surface μ_C period. Then, the subsequent formation of carbides takes a time gap (Δt) of 5.8 min, which is indicated by the relaxation time of the N- and C-related escaped species. Notably, after K^+ modulation, denitrification is delayed to 305 °C, which decreases ΔT to 45 °C, and the carburization process is accelerated since Δt is reduced to 4.7 min (Fig. 3g), which accords with the results obtained for the calculated surface μ_C (Supplementary Fig. 27). Thus, the more matched kinetics of the denitrification–carbonization process enable the carbides to form at a high surface μ_C. To further determine the reason for the matched kinetics, the hydrogenation process of the N site over Fe_2N with and without the K^+ promoter was calculated by DFT (the simulation details are displayed in the computational details section). The modification of K^+ benefits the first N–H bond formation but increases the energy barrier of the second hydrogenation, impeding the entire denitrification process (Fig. 3h and Supplementary Figs. 29–35). In addition, the K^+ promoter benefits surface carbon atom insertion, and the nitrogen atom escapes from the bulk phase (Fig. 3i and Supplementary Figs. 36–40). All these results are summarized in Fig. 3j and emphasize the importance of the K^+ promoter in enhancing surface μ_C to affect denitrification-carbonization kinetics for the controllable construction and stabilization of ε-Fe_2C species under high surface μ_C conditions. Moreover, it should be noted that the direct construction of metastable ε-Fe_2C could be mediated not only by K^+ but also by other alkalies such as Li^+, Na^+, Rb^+, and Cs^+ (Supplementary Fig. 41 and Supplementary Note 11). Additionally, the construction conditions are not confined to Fe_2N annealing in a CO_2-H_2 atmosphere. Fe_2O_3 can also act as an iron precursor and partially evolve into ε-Fe_2C with K^+ modulation in a CO atmosphere (Supplementary Fig. 42 and Supplementary Note 12). Furthermore, under a wide range of temperatures, K^+ and CO_2 concentrations (Supplementary Figs. 43–48 and Supplementary Notes 13–16), the K^+-induced surface chemical potential modulation strategy is capable of inducing the formation of metastable ε-Fe_2C, further confirming its general applicability and potential.

Methodology universality

These aforementioned results of metastable ε-Fe_2C synthesis imply that the modulation of the surface μ_C is an intrinsic factor and is of critical importance for metastable carbide generation via other alkali ion-modulation strategies, such as the use of K+ ions. Thus, to further explore the universality of the proposed strategy and mechanism, molybdenum (Mo)-based metastable species (e.g., γ′-MoC, MoN, and 1*T* chalcogenides) with wide applications were chosen as the target products[40–43]. First, the surface μ_X values of these interstitial atoms (X = O, N, C, S) over Mo with and without the K^+ promoter were further studied via DFT calculations (Supplementary Fig. 49). The DFT results reveal that the addition of K^+ enhances the surface μ_X and then the reaction equilibrium of the corresponding Mo-based materials (Fig. 4a and Supplementary Table 3). The values of $\Delta\mu_{X,\,O}$ with and without K^+ as descriptors of the energy barriers for MoX formation from the MoO_x precursor are displayed in Fig. 4b. The $\Delta\mu_{X,\,O}$ values of X = C and N negatively shift after K^+ modulation, which indicates that the energy barriers for carburization and nitridation from MoO_x are lowered by the K^+ promoter, benefiting the formation and stabilization of metastable Mo-based carbides and nitride species with relatively high carbon or nitrogen contents. In addition, although the changes in the $\Delta\mu_{S,\,O}$ values are not obvious, the $\Delta\mu_S$ after K^+ modulation exhibits the same trend as the $\Delta\mu_C$ and $\Delta\mu_N$, implying that the sulfuration process could also increase thermodynamically, which may also induce the formation of metastable chalcogenide species (Supplementary Table 3). Then, as a proof of concept, MoO_3 and K-MoO_3 were treated under carbonization conditions (Supplementary Fig. 50 and Supplementary Notes 2 and 17). As shown in Fig. 4c, metastable γ′-MoC is successfully obtained from K-MoO_3, whereas when MoO_3 is used as a precursor without the K^+ promoter, only β-Mo_2C can be synthesized

https://doi.org/10.1038/s41467-025-59124-3

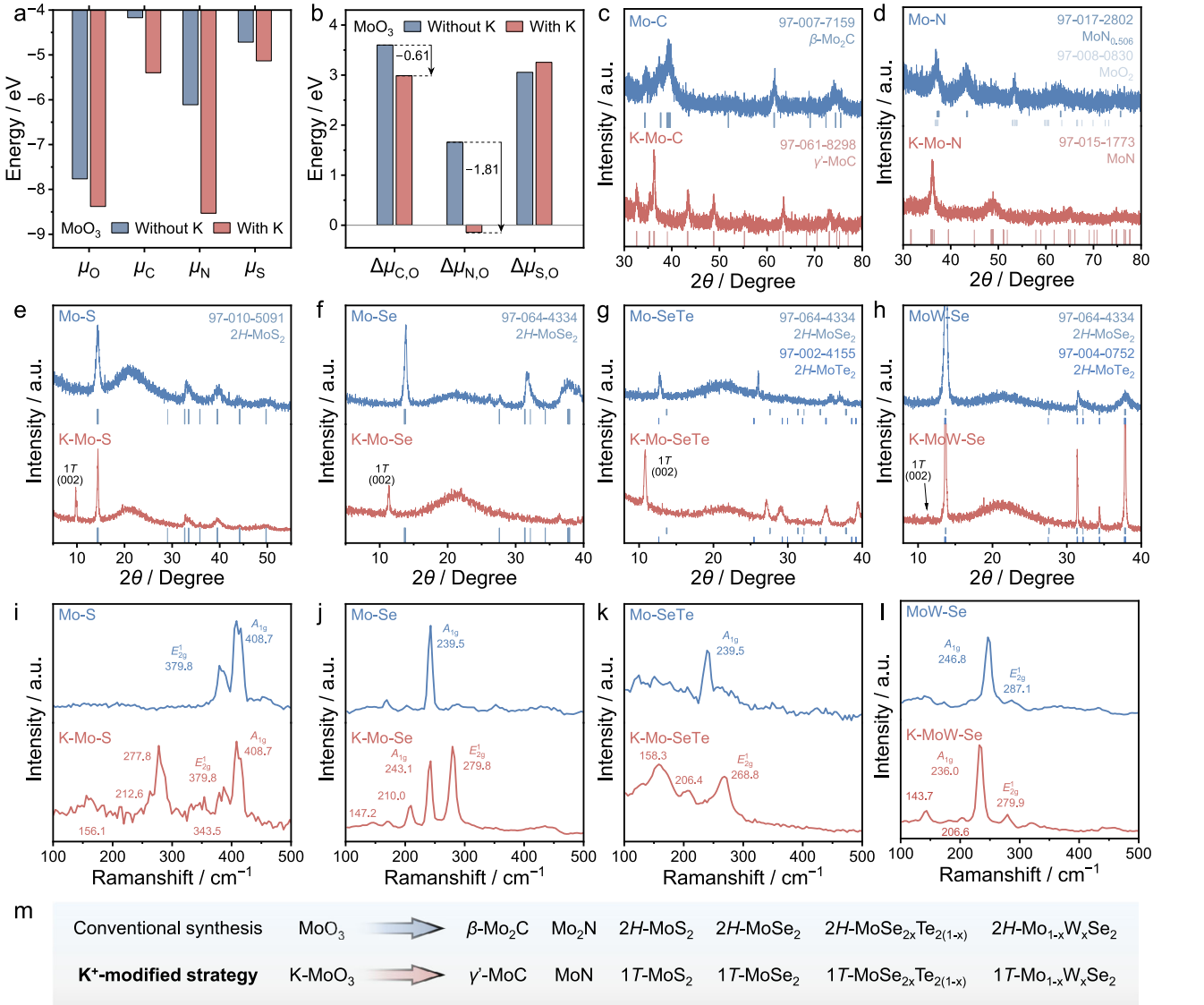

Fig. 4 | Methodology universality. a, **b** Calculation of the chemical potential change of different atoms on the MoO_3 surface with and without K^+. **c**–**l** XRD patterns and Raman spectra of the carbonization, nitrogenization, sulfuration, selenylation, and antimonization of MoO_3 and K-MoO_3. **m** Scheme for the K^+ promoter-mediated construction of the metastable phase. All "a.u." represents arbitrary units.

(Supplementary Figs. 51 and 52 and Supplementary Notes 18 and 19). Similarly, the construction of metastable MoN, 1*T*-MoS_2, 1*T*-$MoSe_2$, 1*T*-$MoSe_{2x}Te_{2(1-x)}$, and 1*T*-$Mo_{1-x}W_xSe_2$ was also achieved over K^+-modified MoO_3 under identical conditions (Fig. 4d–m, Supplementary Figs. 53–63, Supplementary Notes 20–30, and Supplementary Table 4)[44–47], demonstrating the universality of the proposed strategy. Such mechanistic insight might provide a supplementary interpretation for the phase engineering strategy for constructing the 1*T*-Mo(W)S(Se, Te)$_2$ materials proposed by Zhang et al.[2,3].

Proof-of-concept application of the proposed K^+-modulation strategy

The gram-scale synthesis of ε-Fe_2C, MoN, and γ'-MoC could be realized by using a tubular furnace with a diameter of 6 cm (Fig. 5a, Supplementary Fig. 64, and Supplementary Note 31), suggesting its advantages for easy scaling up and considerable application potential. Therefore, to evaluate the stability of metastable ε-Fe_2C, we first studied $\Delta\mu_{O,C}$ theoretically and found that there was a prominent increase in $\Delta\mu_{O,C}$ after K^+ modulation, suggesting that the oxidation resistance of the as-prepared metastable ε-Fe_2C was markedly increased through our strategy (Fig. 5b, c, Supplementary Fig. 65, and Supplementary Table 5). As predicted, the synthesized K-Fe_2C@C exhibited outstanding stability, with the characteristic peaks of ε-Fe_2C remaining distinguishable even when exposed to air for more than 398 days (Fig. 5d, Supplementary Fig. 66, and Supplementary Note 32).

CO_2 hydrogenation was used as a model reaction to evaluate the catalytic potential of the as-prepared metastable ε-Fe_2C materials. As predicted in early reports, K-Fe_2C@C exhibited better CO_2 hydrogenation activity and lower olefin hydrogenation activity than Fe_5C_2@C during transient surface reactions (Supplementary Fig. 67 and Supplementary Note 33). The quantification performance comparison is displayed in Fig. 5e, Supplementary Figs. 68 and 69, and Supplementary Note 34, and Supplementary Table 6. The equilibrium CO_2 conversion rate reached 34.9%, with outstanding $C_2^=$–$C_4^=$ (light olefins) selectivity and O/P ratios of 42.3% and 8.7, respectively, achieved over K-Fe_2C@C, which are obviously greater than those achieved over Fe_5C_2@C (Con. rate, 28.2%; $C_2^=$–$C_4^=$ Sel., 20.4%; O/P, 1.2). Moreover, the performance and morphology of K-Fe_2C@C remained unchanged after the 36 h durability test (Fig. 5f, Supplementary Fig. 70, and Supplementary Note 35), demonstrating the considerable

https://doi.org/10.1038/s41467-025-59124-3

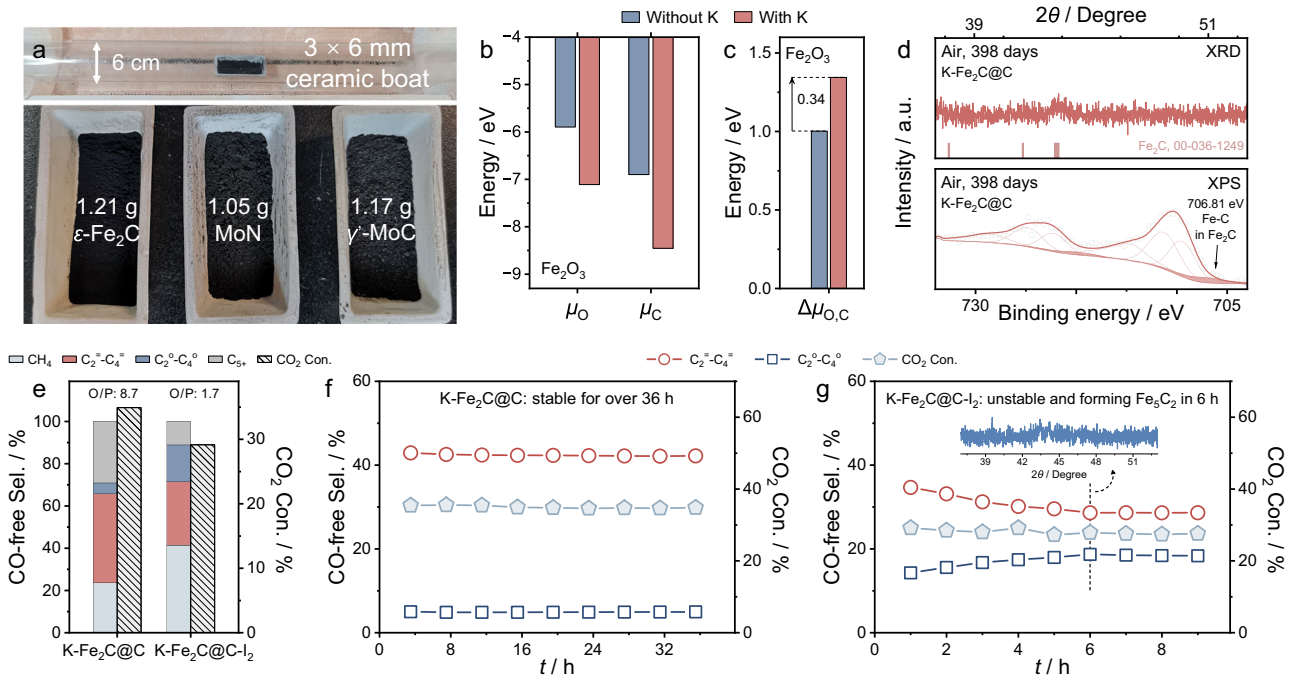

Fig. 5 | Scalable synthesis and a proof-of-concept application. a Verification of the gram-level synthesis. **b.** Calculation of the chemical potential change of O and C on the Fe_2O_3 surface with and without K^+. **c** XRD pattern and XPS Fe 2*p* spectra of K-Fe_2C@C exposed to air for 398 days. **d** Hydrocarbon selectivity and CO_2 conversion rate over K-Fe_2C@C and K-Fe_2C@C-I_2 (the sample in which I_2-acetonitrile was used to remove K from K-Fe_2C@C). "a.u." represents arbitrary units. **e**–**g** CO-free hydrocarbon selectivity and CO_2 conversion over K-Fe_2C@C and K-Fe_2C@C-I_2. Reaction conditions: 300 °C, 1.0 MPa, space velocity = 20,000 mL g^{-1} h^{-1}, H_2/CO_2 = 3. The inset image in **g** is the XRD pattern of the tested K-Fe_2C@C-I_2 after 6 h. "$C_2^=$–$C_4^=$" represents light olefins, "C_2^o–C_4^o" represents light paraffins, "Con." represents conversion, "Sel." represents selectivity, and O/P indicates the olefin/paraffin ratio of C_2–C_4 production. K-Fe_2C@C-I_2 is the sample that uses I_2-acetonitrile to remove K^+ from K-Fe_2C@C.

operating stability of the metastable species obtained from the K^+-modulation strategy. The dynamic mutual transformation of ε-Fe_2C and χ-Fe_5C_2 after removing/re-adding the K^+ promoter during the reaction further verify its crucial effect on metastable construction and stabilization (Fig. 5g, Supplementary Fig. 71, and Supplementary Note 36). Notably, this phenomenon implies the important role of the K^+ promoter in the evolution of metastable active species, which are often overlooked, in the CO_2 hydrogenation process rather than just in electronic structure modification.

Discussion

In summary, modulating the surface carbon chemical potential is theoretically reported to be the crucial factor and descriptor for the synthesis of metastable carbides. A K^+-modulation strategy is subsequently developed to convert iron nitride precursors to metastable ε-Fe_2C. An increased surface carbon chemical potential leads to a better-matched denitriding–carburizing rate and impedes carbon spillover because of the thermodynamically lower formation energy barrier, which kinetically guarantees enhanced stability. Moreover, this K^+-induced surface chemical potential modulation is suitable for the controllable preparation of metastable γ'-MoC, MoN, 1*T*-MoS_2, 1*T*-$MoSe_2$, 1*T*-$MoSe_{2x}Te_{2(1-x)}$, and 1*T*-$Mo_{1-x}W_xSe_2$ from K^+-modified MoO_3 and easy scaling to gram-level synthesis, highlighting the universality and applicability of the methodology. Impressively, metastable ε-Fe_2C can be stable for more than 398 days under an air atmosphere. Furthermore, as a proof of concept, a considerable olefin selectivity of 42.3%, with a lifetime of over 36 h, is achieved during the process of CO_2 hydrogenation over in situ-formed ε-Fe_2C, demonstrating its remarkable operating durability. Our work not only demonstrates a simple surface chemical potential modulation method for constructing highly stable metastable carbides and chalcogenides but also rethinks the real role of alkaline promoters in synthetic and catalytic processes.

Methods

Materials

Iron(III) chloride hexahydrate ($FeCl_3{\cdot}6H_2O$), potassium carbonate (K_2CO_3), dimethylformamide (DMF), and terephthalic acid were purchased from Aladdin Ltd. (Shanghai, China). The mixed gases of carbon dioxide and hydrogen (CO_2/H_2 with a volume ratio of 1/3) and ammonia (NH_3) were purchased from Lian Bo (Tianjin) Co., Ltd. Deionized water (DIW) was used in all the experimental processes. All chemicals were of analytical grade and were used without further purification.

Synthesis of MIL-88 precursors

According to the literature[48], a typical procedure is as follows: First, 0.81 g of $FeCl_3{\cdot}6H_2O$ and 0.50 g of terephthalic acid were dissolved in 50 mL of DMF. The obtained solution was then vigorously stirred for 15 min. Afterward, the mixture was transferred to a Teflon-lined stainless steel autoclave and crystallized for 24 h at 110 °C. Finally, the dark yellow product was harvested by centrifugation, washed with DIW and ethanol several times, and dried in a vacuum oven overnight.

Synthesis of carbon-wrapped iron nitride with (K-Fe_2N@C) and without (Fe_2N@C) K^+ modulation

K-Fe_2N@C was obtained by facile impregnation of K species and subsequent calculations under an NH_3 atmosphere. First, K_2CO_3 was added to a 1 g mL^{-1} solution. Owing to the water absorption of the MIL-88 precursor, 3 μL of potassium solution was added dropwise to 0.1 g of MIL-88 precursor with vigorous stirring until it became sticky. The mixture was subsequently dried at 80 °C, and the obtained powder was placed in a 6 mm diameter quartz tube and put into the tube furnace. The temperature was subsequently increased to 500 °C at a heating rate of 5 °C min^{-1} under an NH_3 atmosphere for 5 h to obtain K-Fe_2N@C. After cooling to room temperature, the sample was sealed

under an Ar atmosphere to prevent oxidation. Fe_2N@C was synthesized via a process similar to that described above without the addition of K species.

Synthesis of carbon-wrapped iron carbide with (K-Fe_2C@C) and without (Fe_5C_2@C) K^+ modulation

K-Fe_2C@C was obtained by in situ carburization under a 25% CO_2/H_2 atmosphere. A 0.3 g sample of sieved (40–80 mesh) K-Fe_2N@C precursor was put into a stainless-steel tube reactor with an inner diameter of 8 mm. Then, the temperature was increased to 350 °C at a heating rate of 5 °C min^{-1} under a 25% CO_2/H_2 atmosphere for approximately 2 h. After cooling to room temperature, the samples could be directly used for subsequent CO_2 hydrogenation or removed for subsequent characterization. In addition, Fe_5C_2@C could be synthesized via a similar process using Fe_2N@C as a precursor.

General characterizations

Powder X−ray diffraction (XRD) was performed on a Bruker D8 Focus Diffraction System (Germany) using a Cu *K*α source (λ = 0.154178 nm). Scanning electron microscopy (SEM) was conducted with an FEI Apreo S LoVac microscope (10 kV). Transmission electron microscopy (TEM) and high-resolution transmission electron microscopy (HRTEM) images were obtained with a JEM-2100F system equipped with an EDAX Genesis XM2. X−ray photoelectron spectroscopy (XPS) measurements were conducted with a PHI-1600 X-ray photoelectron spectrometer equipped with Al *K*α radiation. All the peaks were attributed to the C 1*s* peak at a binding energy of 284.8 eV. Raman spectroscopy was carried out with a Horiba Labram HR Evolution Raman microscope under excitation with a 532 nm laser at a power of 20 mW. Fourier transform infrared spectroscopy (FTIR) was performed on a FEI iS50 instrument. Before analysis, the samples were degassed at 120 °C under vacuum overnight. X−ray absorption fine structure spectroscopy (XAFS) was conducted at the 1W1B station of the Beijing Electron−Positron Collider II (BSRF). The room temperature 57Fe Mössbauer spectra of Fe_5C_2@C and K-Fe_2C@C were recorded under various simulated conditions by using a Topologic 500 A Mössbauer spectrometer with a 57Co (Rh) radiation source and proportional counter detector. The speed was calibrated with *α*-Fe foil, and the absorption thickness of the sample was adjusted to 10 mg Fe cm^{-2}. The analysis of the Mössbauer spectrum was completed on the basis of the Lorentz absorption curve via a computer and MossWinn 3.0i software. Qualitative analysis of the various phases in the catalyst was carried out by fitting the parameters of the isomorphic energy shift (IS), quadrupole splitting (QS), absorption linewidth (LW), and hyperfine field (H_{hf}). The relative content of various iron phases in the catalyst was determined by integrating the absorption peak area of each phase. Nano secondary ion mass spectroscopy (NanoSIMS) was performed on a CAMECA nanoSIMS 50L (France) using a Cs^+ source.

In situ XRD experiments

In situ XRD measurements were conducted on a Smartlab8KW Diffraction System using a Cu *K*α source (λ = 0.154178 nm) with an XRK 900 heater. The experiments were carried out under conditions close to those of the carbonization process, i.e., mixed gas with H_2/CO_2 volume ratios of 3 and 350 °C at ambient pressure for 70 min. Diffraction patterns were recorded within a 2θ range of 30–50° because the most intense diffraction peaks of the relevant phases, i.e., Fe_2N, Fe_2C, and Fe_5C_2, mainly fall in this range. The scanning rate was 20°/min.

In situ DRTIFTS measurements

In situ DRIFTS measurements were conducted in continuous flow mode under an atmosphere of mixed H_2 and CO_2 gas with a volume ratio of 3. Specifically, the catalysts and anhydrous KBr were ground together at a ratio of 1/5 and degassed at 450 °C under a He atmosphere for 2 h. Then, *T* was decreased to 350 °C, and the reaction gases (H_2 and CO_2 with a ratio of 4/1) were introduced into the reactor. Next, the background spectrum was collected under the same conditions, and the spectrum was recorded as a function of time to monitor the intermediates adsorbed on the catalyst surface during the on-stream reaction.

In situ Raman analysis

In situ Raman spectroscopy was performed via a Raman microscopy system (LabRAM HR Evolution, Horiba Jobin Yvon) with a 532 nm Ar ion laser beam. The powdered sample was added to the reactor, which was ramped up to 450 °C with N_2 for 2 h to degas. Afterward, *T* was decreased to 350 °C, and a 25% CO_2/H_2 atmosphere was introduced into the reactor for spectrum acquisition.

TPD/TPSR-MS experiments

TPD/TPSR-MS experiments were carried out in a TP-5076 characterization system (Xianquan Co., Ltd., Tianjin, China), and a QAS mass spectrometer (Linglu Instruments, Shanghai, China) was used to analyze the reactants and products online. The *m*/*z* values detected were as follows: 2 for H_2, 14 for the released N species, 28 for ethylene, 30 for ethane, and 44 for CO_2. For CO-TPD, approximately 100 mg of catalyst was first treated under an Ar flow (20 mL/min) at 60 °C for 30 min, degassed at 300 °C for 2 h using a 20 mL/min Ar flow, and then cooled to room temperature. The sample was purged with 10% CO/Ar mixed gas (20 mL/min) for 1 h under ambient conditions. After adsorption saturation, the sample was heated to 450 °C under an Ar flow (20 mL/min) at a rate of 10 °C min^{-1}. The amount of CO flowing out of the sample was monitored by a thermal conductivity detector (TCD). For the TPSR-MS analysis, the same amount of catalyst was first degassed for the CO-TPD measurements. Then, the temperature was decreased to 60 °C, and the sample was exposed to 25% CO_2/H_2 (20 mL/min) at 60 °C for approximately 15 mins. After that, the catalyst was heated to 350 °C at a rate of 10 °C min^{-1}. The tail gas was monitored by MS.

Computational details

In this work, all DFT calculations were performed via the Vienna Ab initio Simulation Package (VASP). The projector augmented wave (PAW) pseudopotential with the PBE generalized gradient approximation (GGA) exchange correlation function was utilized in the computations. The cut-off energy of the plane wave basis set was 500 eV, and a Monkhorst-Pack mesh of $3 \times 3 \times 1$ was used for K-sampling in the adsorption energy calculation. The long-range dispersion interaction was described via the DFT-D3 method. All the atoms were fully relaxed with an energy convergence tolerance of 10^{-5} eV per atom, and the final force on each atom was <0.01 eV $Å^{-1}$. The TS searches were performed via the Dimer method in the VTST package. The final force on each atom was <0.05 eV $Å^{-1}$. The TS search is conducted by using the climbing-image nudged elastic band (CI-NEB) method to generate initial guess geometries, followed by the dimer method to converge to the saddle points.

The adsorption energy of the reaction intermediates can be computed via Eqs. (1 and 2):

$$\Delta E = E_{(ads/slab)} - E_{ads} - E_{slab} \quad (1)$$

$$\Delta G = \Delta E + \Delta E_{ZPE} - T\Delta S \quad (2)$$

where ΔE_{ZPE} is the zero-point energy change and ΔS is the entropy change. In this work, the values of ΔE_{ZPE} and ΔS are obtained via vibration frequency calculations via vaspkit[49]. Visuals were produced with VESTA[50] and Blender.

To simplify the calculation process, we did not consider the adsorption and desorption processes of molecules such as CO_2 and H_2

here, but focused on the surface reaction process. H_2 is believed to decompose into *H and adsorb on the surface before the reaction. Owing to the presence of 50% unfilled N vacancies on the Fe_2N surface, CO_2 can be reduced to C in the unfilled vacancies, while the N sites can be further hydrogenated to NH_3 and escape from Fe_2N precursors. Thus, the whole conversion process of iron nitrides to the corresponding carbides is decoupled into two processes for convenient simulation: the surface N sites of Fe_2N are gradually hydrogenated to NH_3 and escape, and then the *C formed through CO_2 permeates into the sublayer for the formation of iron carbides. The energy of the reaction can be calculated via Eqs. (3–15):

$$* + CO_2 + 4*H \rightarrow *CO_2 + 4*H \quad (3)$$

$$*CO_2 + 4*H \rightarrow *COOH + 3*H\,(TS1) \quad (4)$$

$$*COOH + 3*H \rightarrow *CO + *H_2O + 2*H\,(TS2) \quad (5)$$

$$*CO + *H_2O + 2*H \rightarrow *COH + *H_2O + *H\,(TS3) \quad (6)$$

$$*COH + *H_2O + *H \rightarrow *C + *OH + *H_2O\,(TS4) \quad (7)$$

$$*C + *OH + *H_2O \rightarrow *C + 2*H_2O\,(TS5) \quad (8)$$

$$*CO_2 + 4*H \rightarrow *CO + *H_2O + 2*H\,(TS6) \quad (9)$$

$$*CO + *H_2O + 2*H \rightarrow *C + 2*H_2O\,(TS7) \quad (10)$$

$$*N + 3*H \rightarrow *NH + 2*H\,(TS8) \quad (11)$$

$$*NH + 2*H \rightarrow *NH_2 + *H\,(TS9) \quad (12)$$

$$*NH_2 + *H \rightarrow *NH_3\,(TS10) \quad (13)$$

$$*N_{bulk} \rightarrow *N_{surface}\,(TS11) \quad (14)$$

$$*C_{surface} \rightarrow *C_{bulk}\,(TS12) \quad (15)$$

Performance evaluation

Flow reactor studies of CO_2 hydrogenation were performed in a stainless steel tube reactor with an inner diameter of 8 mm under a pressure of 1 MPa. For the steady-state experiments, 300 mg of sieved catalyst (40–80 mesh) was loaded into a reactor tube and held in place by quartz wool. The temperature was increased to 300 °C at a rate of 10 °C/min, and the samples were pretreated in the presence of reactants (36 mL min^{-1} CO_2 + 144 mL min^{-1} H_2). The gas was then changed to pure N_2 for degassing. After that, the reactants were introduced again. Finally, the products were subjected to a GC-2014 gas chromatograph equipped with a PLOT-Q column (with Ar as the carrier gas) and a flame ionization detector (FID) for analysis of the C_1–C_8 hydrocarbons. For CO, CO_2, and N_2, a thermal conductivity detector (TCD) with a 5 A molecular sieve column was used. The evolution rates of different products and CO_2 conversion rates were determined via Eqs. (16) and (17). All the experiments were repeated three times.

$$\text{Evolution Rate}(\mu mol/g/s) = (\text{peak area of X} \times C)/(\text{peak area of standard gas} \times m) \times F_X \quad (16)$$

$$CO_2\text{Conversion}(\%) = (\text{peak area of B} - \text{peak area of A})/(\text{peak area of B}) \quad (17)$$

X: Different products, including H_2, CO, and C_1–C_8 hydrocarbons.*C*: The concentration of X in standard gas. *m*: The mass of the catalyst used. *A*: The area of the CO_2 outlet; B: The area of the CO_2 inlet. F_X: The flow rate of X.

Reporting summary

Further information on research design is available in the Nature Portfolio Reporting Summary linked to this article.

Data availability

The data that support other plots within this paper are available from the corresponding author upon request. The source data underlying Figs. 1–5 are provided as a Source Data file. Source data are provided with this paper.

References

1. Kappera, R. et al. Phase-engineered low-resistance contacts for ultrathin MoS_2 transistors. *Nat. Mater.* **13**, 1128–1134 (2014).
2. Lai, Z. et al. Metastable 1T′-phase group VIB transition metal dichalcogenide crystals. *Nat. Mater.* **20**, 1113–1120 (2021).
3. Yu, Y. et al. High phase-purity 1T′-MoS_2- and 1T′-$MoSe_2$-layered crystals. *Nat. Chem.* **10**, 638–643 (2018).
4. Li, Z. et al. 1T′-transition metal dichalcogenide monolayers stabilized on 4H-Au nanowires for ultrasensitive SERS detection. *Nat. Mater.* **23**, 1355–1362 (2024).
5. Zhang, X. et al. A stable low-temperature H_2-production catalyst by crowding Pt on α-MoC. *Nature* **589**, 396–401 (2021).
6. Liu, W. et al. A durable and pH-universal self-standing MoC–Mo_2C heterojunction electrode for efficient hydrogen evolution reaction. *Nat. Commun.* **12**, 6776 (2021).
7. Qian, F. et al. Stabilized ε-Fe_2C catalyst with Mn tuning to suppress C_1 byproduct selectivity for high-temperature olefin synthesis. *Nat. Commun.* **15**, 5128 (2024).
8. Wang, P. et al. Synthesis of stable and low-CO_2 selective ε-iron carbide Fischer–Tropsch catalysts. *Sci. Adv.* **4**, eaau2947 (2018).
9. Lyu, S. et al. Stabilization of ε-iron carbide as high-temperature catalyst under realistic Fischer–Tropsch synthesis conditions. *Nat. Commun.* **11**, 6219 (2020).
10. Sokolikova, M. S. & Mattevi, C. Direct synthesis of metastable phases of 2D transition metal dichalcogenides. *Chem. Soc. Rev.* **49**, 3952–3980 (2020).
11. Du, Z. et al. Conversion of non-van der Waals solids to 2D transition-metal chalcogenides. *Nature* **577**, 492–496 (2020).
12. Sandoval-Diaz, L. et al. Metastable nickel–oxygen species modulate rate oscillations during dry reforming of methane. *Nat. Catal.* **7**, 161–171 (2024).
13. Sidhik, S. et al. Two-dimensional perovskite templates for durable, efficient formamidinium perovskite solar cells. *Science* **384**, 1227–1235 (2024).
14. Oh, S.-H. et al. Predictive synthesis of transition metal carbide via thermochemical oxocarbon equilibrium. *J. Am. Chem. Soc.* **146**, 17940–17955 (2024).
15. Xin, H. et al. Reverse water gas-shift reaction product driven dynamic activation of molybdenum nitride catalyst surface. *Nat. Commun.* **15**, 3100 (2024).
16. Liu, X., Liu, J., Yang, Y., Li, Y.-W. & Wen, X. Theoretical perspectives on the modulation of carbon on transition-metal catalysts for conversion of carbon-containing resources. *ACS Catal.* **11**, 2156–2181 (2021).
17. Xiao, T. et al. Nanocrystals with metastable high-pressure phases under ambient conditions. *Science* **377**, 870–874 (2022).

18. Liang, J. et al. Gas-balancing adsorption strategy towards noble-metal-based nanowire electrocatalysts. *Nat. Catal*. https://doi.org/10.1038/s41929-024-01167-8 (2024).
19. de Smit, E. et al. Stability and reactivity of ϵ−χ−θ iron carbide catalyst phases in Fischer–Tropsch synthesis: controlling μC. *J. Am. Chem. Soc.* **132**, 14928–14941 (2010).
20. Shrestha, A., Gao, X., Hicks, J. C. & Paolucci, C. Nanoparticle size effects on phase stability for molybdenum and tungsten carbides. *Chem. Mater.* **33**, 4606–4620 (2021).
21. Zhao, B. et al. Unveiling the activity origin of iron nitride as catalytic material for efficient hydrogenation of CO_2 to C_{2+} hydrocarbons. *Angew. Chem. Int. Ed.* **60**, 4496–4500 (2021).
22. Zhu, J. et al. Dynamic structural evolution of iron catalysts involving competitive oxidation and carburization during CO_2 hydrogenation. *Sci. Adv.* **8**, eabm3629 (2022).
23. Niu, L. et al. In situ XRD study on promotional effect of potassium on carburization of spray-dried precipitated Fe_2O_3 catalysts. *ChemCatChem* **9**, 1691–1700 (2017).
24. Wang, D., Xie, Z., Porosoff, M. D. & Chen, J. G. Recent advances in carbon dioxide hydrogenation to produce olefins and aromatics. *Chem* **7**, 2277–2311 (2021).
25. Wang, M. et al. Stabilizing Co_2C with H_2O and K promoter for CO_2 hydrogenation to C_{2+} hydrocarbons. *Sci. Adv.* **9**, eadg0167 (2023).
26. Niu, L. et al. Genesis of an Fe_5C_2@Fe_3O_4 core/shell structure during CO carburization of metallic iron nanoparticles. *J. Catal.* **407**, 97–103 (2022).
27. Xu, J. et al. Highly selective production of long-chain aldehydes, ketones or alcohols via syngas at a mild condition. *Appl. Catal. B* **307**, 121155 (2022).
28. Fu, X.-P. et al. Supported Fe_2C catalysts originated from Fe_2N phase and active for Fischer–Tropsch synthesis. *Appl. Catal. B* **284**, 119702 (2021).
29. Chai, J. et al. The role of H_2 in Fe carburization by CO in Fischer–Tropsch catalysts. *J. Catal.* **400**, 93–102 (2021).
30. Zhao, H. et al. Synthesis of iron-carbide nanoparticles: identification of the active phase and mechanism of Fe-based Fischer–Tropsch synthesis. *CCS Chem.* **3**, 2712–2724 (2021).
31. Chang, Q. et al. XAFS studies of Fe–SiO_2 Fischer–Tropsch catalyst during activation in CO, H_2, and synthesis gas. *ChemCatChem* **11**, 2206–2216 (2019).
32. Paalanen, P. P., van Vreeswijk, S. H., Dugulan, A. I. & Weckhuysen, B. M. Identification of iron carbides in Fe(–Na–S)/α-Al_2O_3 Fischer–Tropsch synthesis catalysts with X-ray powder diffractometry and mössbauer absorption spectroscopy. *ChemCatChem* **12**, 5121–5139 (2020).
33. Have, I. C. T. et al. Uncovering the reaction mechanism behind CoO as active phase for CO_2 hydrogenation. *Nat. Commun* **13**, 324 (2022).
34. Wu, Q. et al. Surface intermediates steer the pathways of CO_2 hydrogenation on Pt/γ-Al_2O_3: Importance of the metal-support interface. *J. Catal.* **425**, 40–49 (2023).
35. Kattel, S., Yan, B., Yang, Y., Chen, J. G. & Liu, P. Optimizing binding energies of key intermediates for CO_2 hydrogenation to methanol over oxide-supported copper. *J. Am. Chem. Soc.* **138**, 12440–12450 (2016).
36. Singh, M., Zhou, N., Paul, D. K. & Klabunde, K. J. IR spectral evidence of aldol condensation: acetaldehyde adsorption over TiO_2 surface. *J. Catal.* **260**, 371–379 (2008).
37. Wen, W., Yan, P., Sun, W., Zhou, Y. & Yu, X.-Y. Metastable phase Cu with optimized local electronic state for efficient electrocatalytic production of ammonia from nitrate. *Adv. Funct. Mater.* **33**, 2212236 (2023).
38. Kani, N. C. et al. Electrochemical reduction of nitrates on CoO nanoclusters-functionalized graphene with highest mass activity and nearly 100% selectivity to ammonia. *Adv. Energy Mater.* **13**, 2204236 (2023).
39. Schenkman, K. A., Marble, D. R., Burns, D. H. & Feigl, E. O. Myoglobin oxygen dissociation by multiwavelength spectroscopy. *J. Appl. Physiol.* **82**, 86–92 (1997).
40. Jin, H. et al. Molten salt-directed catalytic synthesis of 2D layered transition-metal nitrides for efficient hydrogen evolution. *Chem* **6**, 2382–2394 (2020).
41. Qian, X. et al. Quantum spin hall effect in two-dimensional transition metal dichalcogenides. *Science* **346**, 1344–1347 (2014).
42. Jin, H., Song, T., Paik, U. & Qiao, S.-Z. Metastable two-dimensional materials for electrocatalytic energy conversions. *Acc. Mater. Res.* **2**, 559–573 (2021).
43. Chen, J. G. Carbide and nitride overlayers on early transition metal surfaces: preparation, characterization, and reactivities. *Chem. Rev.* **96**, 1477–1498 (1996).
44. Ye, C. et al. A Mo_5N_6 electrocatalyst for efficient Na_2S electrodeposition in room-temperature sodium-sulfur batteries. *Nat. Commun.* **12**, 7195 (2021).
45. Yin, Y. et al. Synergistic phase and disorder engineering in 1T-$MoSe_2$ nanosheets for enhanced hydrogen-evolution reaction. *Adv. Mater.* **29**, 1700311 (2017).
46. Sarkar, A., Sanyal, G., Chakraborty, B. & Show, B. Phase engineering of molybdenum dichalcogenide to anion-tunable polyphasic quaternary chalcogenide (2H/1T/1T') $MoS_xSe_yTe_z$ ($x + y + z = 2$) amplifies the growth of H_2 electrolytically. *ACS Appl. Energy Mater.* **6**, 8017–8031 (2023).
47. Yun, S. J. et al. Telluriding monolayer MoS_2 and WS_2 via alkali metal scooter. *Nat. Commun.* **8**, 2163 (2017).
48. Wang, L. et al. The MIL-88A-derived Fe_3O_4-carbon hierarchical nanocomposites for electrochemical sensing. *Sci. Rep.* **5**, 14341 (2015).
49. Wang, V. et al. VASPKIT: a user-friendly interface facilitating high-throughput computing and analysis using VASP code. *Comput. Phys. Commun.* **267**, 108033 (2021).
50. Momma, K. & Izumi, F. VESTA 3 for three-dimensional visualization of crystal, volumetric and morphology data. *J. Appl. Crystallogr.* **44**, 1272–1276 (2011).
51. Marín-Yaseli, M. R., Moreno, M., de la Fuente, J. L., Briones, C. & Ruiz-Bermejo, M. Experimental conditions affecting the kinetics of aqueous HCN polymerization as revealed by UV–vis spectroscopy. *Spectrochim. Acta A* **191**, 389–397 (2018).
52. Eicher, J. J., Snoep, J. L. & Rohwer, J. M. Determining enzyme kinetics for systems biology with nuclear magnetic resonance spectroscopy. *Metabolites* **2**, 818–843 (2012).

Acknowledgements

The authors are grateful to the National Key Research and Development Program of China (2024YFA1510100 to B.Z. and B.-H.Z.) and the National Natural Science Foundation of China (22209120 to B.-H.Z. and 21871206 to B.Z.). This work is also supported by the Fundamental Research Funds for the Central Universities of China and the 1W1B beamline of the Beijing Synchrotron Radiation Facility.

Author contributions

B.Z. and B.-H.Z. conceived and directed the research. F.C., B.-H.Z. and B.Z. designed the experiments. F.C. synthesized the materials and carried out most of the experiments. Y.H. and J.W. assisted with the experiments. C.C. contributed to the theoretical calculations. F.C., B.-H.Z. and B.Z. analyzed the data. F.C., C.C., and B.-H.Z. wrote the paper. B.Z. revised the paper with comments from all the authors.

Competing interests

The authors declare no competing interests.

Additional information

Supplementary information The online version contains supplementary material available at https://doi.org/10.1038/s41467-025-59124-3.

Correspondence and requests for materials should be addressed to Bo-Hang Zhao or Bin Zhang.

Peer review information *Nature Communications* thanks the anonymous reviewers for their contribution to the peer review of this work. A peer review file is available.